Supplementary Information

for

Camera-Based Localization Microscopy Optimized with Calibrated Structured Illumination

Martin Schmidt[+], Adam C. Hundahl[+], Henrik Flyvbjerg[+], Rodolphe Marie[+] & Kim I. Mortensen[+*]

[+] Department of Health Technology, Technical University of Denmark, Kongens Lyngby, DK-2800, Denmark

January 18, 2021

*Corresponding author: kimo@dtu.dk

Contents

List of Supplementary Figures

Supplementary Note 1: Image formation

Consider a microscopy image of an isolated, fluorescent point-source, and the theory for the spatial intensity distribution it produces on the camera. The probability density to observe a source photon at position $\vec{r}$ on the camera is given by the point spread function (PSF) of the microscope $p_{\mathrm{PSF}}(\vec{r}|\theta_{\mathrm{PSF}})$. Here θ_{PSF} is a set of parameters that specifies the PSF, which, typically, includes at least the position coordinates of the fluorescent point-source. The probability p_i for measuring a source photon in the i'th pixel of the camera is

$$p_i(\theta_{\mathrm{PSF}}) = \int_{\vec{r}\in \text{ pixel\#i}} d\vec{r}\, p_{\mathrm{PSF}}(\vec{r}|\theta_{\mathrm{PSF}}) \ . \tag{S1}$$

In an image of the point-source, we denote the expected total number of source photons by $\langle N\rangle$ and the expected number of background photons in each pixel by $\langle b^2\rangle$. We assume that the latter is constant across the relevant part of the image.

Our theory for the expected value $E_i = \langle n_i\rangle$ of the number of photons n_i detected with the i'th pixel on the camera in a single image is

$$E_i(\theta) = \langle N\rangle\, p_i(\theta_{\mathrm{PSF}}) + \langle b^2\rangle \ . \tag{S2}$$

Here θ is a set of parameters to be estimated from data, which includes all parameters θ_{PSF}, necessary to specify the PSF, along with the total photon number, and the constant background, i.e. $\theta = \theta_{\mathrm{PSF}} \cup \{\langle N\rangle, \langle b^2\rangle\}$.

Although notable exceptions exist [7, 8], often, in localization microscopy, a 2D-Gaussian approximation to the theoretical PSF is assumed. Consequently,

$$p_{\mathrm{PSF}}(\vec{r}|\theta_{\mathrm{PSF}}) = \frac{1}{2\pi\sigma_{\mathrm{PSF}}^2}\, e^{-(\vec{r}-\vec{\mu})^2/2\sigma_{\mathrm{PSF}}^2} \ , \tag{S3}$$

such that $\theta_{\mathrm{PSF}} = \{\vec{\mu}, \sigma_{\mathrm{PSF}}\}$ is comprised of the point-source's 2D position coordinates $\vec{\mu}$ and the width of the Gaussian parametrized as its spatial s.d. σ_{PSF}. This assumption is indeed valid, if the plateaus of the actual PSF's slowly decaying tails surrounding its central peak are modelled as "background" and the localization analysis is restricted to this vicinity [5]. Thus, we admit contributions to the spatially constant background from (i) a term proportional to the excitation intensity, since this light stems from the point-source; and (ii) a term that quantifies any other background independent of the laser intensity.

We assume that photons superpose incoherently to form the image of a point-source. Consequently, the number n_i of photons detected with pixel i on the camera is Poisson distributed,

$$p_i(n_i) = e^{-E_i}\, \frac{E_i^{n_i}}{n_i!} \ . \tag{S4}$$

Note that all parameter dependencies are contained in $E_i = E_i(\theta)$ as given by equation (S2). Note finally that, in practice, the pixel output values from the camera are not actual photon counts but signal values that have been produced after EM amplification in the EMCCD camera and addition of a constant offset value [6]. The amplification process, essentially, causes all variances to be doubled, which we account for when we compare experimentally obtained sample variances to theory throughout the present work. In computer-simulated experiments (see below), however, we use photon statistics for simplicity.

Supplementary Note 2: Conventional localization with a single image

We point the reader to Ref. [5] for a thorough treatment and comparison of methods for localization of point-sources in fluorescence microscopy using fitting of PSFs. Here, we follow that framework and notation, where possible. Briefly, the optimal image analysis based on a single image uses Maximum Likelihood Estimation (MLE) in conjunction with a sufficiently accurate model for the PSF. In MLE, the parameters θ are estimated by maximization of the likelihood w.r.t. θ based on the image data in the form of pixel photon counts $\{n_i\}_i \equiv \{n_i\}_{i=1,\ldots,N_{\text{pixels}}}$. Here, N_{pixels} is the number of pixels surrounding the spot, which are used for analysis. The likelihood for the parameters θ is

$$\mathcal{L}(\theta|\{n_i\}_i) = P(\{n_i\}_i|\theta) \ , \tag{S5}$$

and thus mathematically equal to the joint probability $P(\{n_i\}_i|\theta)$ for observing $\{n_i\}_i$ given the parameters θ. Since pixels in the image are statistically independent,

$$P(\{n_i\}_i|\theta) = \prod_{i=1}^{N_{\text{pixels}}} p_i(n_i) \ . \tag{S6}$$

The ML estimate of θ and thus the position of the point-source may be found by maximization of the left-hand side of equation (S5) w.r.t. θ, or alternatively, and often more tractable, by maximization of the log-likelihood $\ell = \log(\mathcal{L})$. Furthermore, the errorbar of a position estimate thus obtained may be found as a function of θ [5]. In the relevant case where a 2D-Gaussian-plus-a-constant is a sufficiently accurate approximation of the actual PSF, the errorbar may be found from equation (5) in Ref. [5].

Supplementary Note 3: Localization with multiple images

In the case where multiple images of a point-source have been acquired, its position may be determined from each individual image, as described above. This might fail, however, if some images contain too few source photons to permit its separate analysis. If the point-source moves negligibly within the duration of acquisition, instead, all N_{images} images may be analyzed simultaneously to determine the position. This permits analysis also of low-intensity images, provided that the sum of source photons in images is sufficiently large. Neither the point-source position $\vec{\mu}$ nor the PSF width σ_{PSF} depends on the image number, but consider the pertinent situation where images have been acquired with different excitation intensities. Thus, we denote expected total photon numbers by $\langle N_j \rangle$ and expected numbers of background photons per pixel by $\langle b_j^2 \rangle$, where $j = 1, \ldots, N_{\text{images}}$ specifies the image number. In this analysis $\theta = \{\vec{\mu}, \sigma_{\text{PSF}}^2, \langle N_1 \rangle, \ldots, \langle N_{N_{\text{images}}} \rangle, \langle b_1^2 \rangle, \ldots, \langle b_{N_{\text{images}}}^2 \rangle\}$, constituting $3 + 2N_{\text{images}}$ parameters that must be determined with MLE.

Assume that $n_{i,j}$ photons have been detected with the camera's i'th pixel in the j'th image. Since all pixels in each image and all images are statistically independent, the likelihood reads

$$\mathcal{L}(\theta|\{n_{i,j}\}_{i,j}) = \prod_{j=1}^{N_{\text{images}}} \prod_{i=1}^{N_{\text{pixels}}} e^{-E_{i,j}} \frac{E_{i,j}^{n_{i,j}}}{n_{i,j}!} \quad , \tag{S7}$$

where $E_{i,j} = \langle n_{i,j} \rangle$. In practice, one instead maximizes the log-likelihood,

$$\ell = \sum_{j=1}^{N_{\text{images}}} \sum_{i=1}^{N_{\text{pixels}}} [-E_{i,j} + n_{i,j} \log E_{i,j}] \quad , \tag{S8}$$

w.r.t. θ. Note that in the case of camera-based localization either with a single or multiple images, the point-source position $\vec{\mu}$ enters the likelihood only through the PSF as in equation (S3). That is, neither $\langle N_j \rangle$ nor $\langle b_j^2 \rangle$ depends on $\vec{\mu}$ in this paradigm.

Supplementary Note 4: Camera-based MINFLUX

In the paradigm of MINFLUX [1], a fluorescent point-source is localized by counting emitted photons with a photo-multiplier tube under a doughnut-shaped illumination beam placed at multiple positions in the vicinity of the point-source. The scanning configuration and need for feedback-control of the illumination relative to the point-source, however, limited throughput.

As discussed in the main text, this information component about a point-source's position, however, may be accessed also in camera-based localization microscopy under structured illumination, as previously demonstrated in SIMPLE [10], SIMFLUX [2] and ROSE [4]. To appreciate this strategy, consider the simple case where a fluorescent point-source is exposed sequentially to two different field-wide excitation light structures. We assume that the point-source moves negligibly between the exposures and, for simplicity, that the duration of exposures is identical. To keep notation simple, we consider here localization in 1D. Unless the excitation light intensities are constant in space, the expected total numbers of photons detected from the point-source depend on its position μ_x relative to the exciting light structures. Thus,

$$\langle N_1 \rangle = \nu_1(\mu_x) \tag{S9}$$

$$\langle N_2 \rangle = \nu_2(\mu_x) \quad . \tag{S10}$$

Furthermore, if the two excitation light intensity structures are created by simple translation (phase shift) of the same structure, f, by a distance L along the axis, the expected total photon numbers have simple dependencies on the position of the point-source. With proper choice of origin of the axis,

$$\nu_1(\mu_x) = I f(\mu_x) \tag{S11}$$

$$\nu_2(\mu_x) = I f(\mu_x + L) \quad , \tag{S12}$$

where the common scale factor I parameterizes the photo-physics of the excitation-emission processes, laser intensity, detection efficiency, and duration of exposure.

In a camera-based MINFLUX experiment of the type described above, one measures the number of photons N_1 and N_2, respectively, detected from the point-source during each of the two exposures. Those values may, e.g., be determined as an integral part of camera-based localization analysis, as described above and in the main text. Regardless of how they were measured, N_1 and N_2 are Poisson-distributed random variables, and they are statistically independent. Therefore, the joint probability for measuring the set of values $\{N_1, N_2\}$ is the product of the individual probabilities, given the parameters μ_x and I, i.e.,

$$P(\{N_1, N_2\}|\mu_x, I) = e^{-\nu_1} \frac{\nu_1^{N_1}}{N_1!} e^{-\nu_2} \frac{\nu_2^{N_2}}{N_2!} \ . \tag{S13}$$

To localize a point-source using camera-based MINFLUX, μ_x may be determined systematically using MLE. To this end, the likelihood of μ_x (and I) given the data $\{N_1, N_2\}$,

$$\mathcal{L}(\mu_x, I|\{N_1, N_2\}) = P(\{N_1, N_2\}|\mu_x, I) \ , \tag{S14}$$

is maximized with respect to μ_x. Alternatively, one may maximise its logarithm, $\ell = \log \mathcal{L}$,

$$\ell = -\nu_1 + N_1 \log(\nu_1) - \nu_2 + N_2 \log(\nu_2) \ , \tag{S15}$$

in which we have omitted terms that do not depend on μ_x. Note here that the stationarity condition with respect to μ_x does not depend on I.

While not required, typically, in a wide-field configuration, the illumination structures will be periodic. In that case, this data analysis determines only the position of the point-source *relative* to *a period* of the structured illumination. However, combining MINFLUX-based localization with fitting of PSFs (ROSE [4], SIMFLUX [2], C-MELM) or other image analysis (SIMPLE [10]), eliminates this ambiguity.

Supplementary Note 5: Variance of camera-based MINFLUX estimates

Maximum likelihood estimates are optimal in the sense that they are asymptotically unbiased and efficient for sufficiently good statistics [9]. Thus, in this limit, MLE yields the correct value on average and has the lowest possible variance among unbiased estimators. The covariance matrix of the estimator may be calculated as the inverse of Fisher's information matrix $\mathcal{I}$ with elements

$$\mathcal{I}_{i,j} = -\left\langle \frac{\partial^2 \ell}{\partial \theta_i \theta_j} \middle| \vec{\theta} \right\rangle \ , \tag{S16}$$

where θ_i and θ_j are parameters in θ, and the expected value is evaluated with respect to the joint probability density of the measurements. In particular, for camera-based MINFLUX in 1D with images acquired with identical exposure time under structured illumination, $\theta = \{\mu_x, I\}$, for example, Fisher's information matrix may be calculated as

$$\mathcal{I}_{1,1} = -\left\langle \frac{\partial^2 \ell}{\partial \mu_x^2} \middle| \vec{\theta} \right\rangle = \frac{1}{\nu_1} \left(\frac{\partial \nu_1}{\partial \mu_x} \right)^2 + \frac{1}{\nu_2} \left(\frac{\partial \nu_2}{\partial \mu_x} \right)^2 \tag{S17}$$

$$\mathcal{I}_{1,2} = \mathcal{I}_{2,1} = -\left\langle \frac{\partial^2 \ell}{\partial \mu_x \partial I} \middle| \vec{\theta} \right\rangle = \frac{1}{I} \left(\frac{\partial \nu_1}{\partial \mu_x} + \frac{\partial \nu_2}{\partial \mu_x} \right) \tag{S18}$$

$$\mathcal{I}_{2,2} = -\left\langle \frac{\partial^2 \ell}{\partial I^2} \middle| \vec{\theta} \right\rangle = \frac{\nu_1 + \nu_2}{I^2} \ . \tag{S19}$$

Given an excitation illumination structure, the derivatives of the expected photon numbers may be calculated analytically or numerically and the covariance matrix of the ML estimator may be obtained as the inverse of $\mathcal{I}$. Variances of camera-based MINFLUX estimates in 2D follow as a straight-forward extension of this.

Supplementary Note 6: Camera-based MINFLUX with harmonic illumination

As a simple example of camera-based MINFLUX, we consider a case where the excitation light is two harmonic structures with identical wavelength λ—and hence identical wave number $k = 2\pi/\lambda$—and maximal intensity I, but one shifted spatially $L = \lambda/4$ relatively to the other. With proper choice of origin of the x-axis, their intensities read

$$\begin{aligned} I_1(x) &= I\cos^2(kx) && \text{(S20)} \\ I_2(x) &= I\sin^2(kx)\ . && \text{(S21)} \end{aligned}$$

When excited, the number of photons emitted by the fluorescent point-source is stochastic, Poisson distributed, with expected value proportional to the intensity and duration of the excitation as in equations (S11) and (S12). Let again μ_x denote the location of the fluorescent point-source on the x-axis. When it is excited with the two illumination structures for identical durations, the expected numbers of photons, $\langle N_1\rangle$ and $\langle N_2\rangle$, recorded from the point-source are, respectively,

$$\begin{aligned} \nu_1 &= \langle N_1\rangle = \nu\cos^2(k\mu_x) && \text{(S22)} \\ \nu_2 &= \langle N_2\rangle = \nu\sin^2(k\mu_x)\ , && \text{(S23)} \end{aligned}$$

where $\nu \equiv \langle N\rangle = \langle N_1 + N_2\rangle = I$ is the expected value of the total number of recorded source photons in the two images. For our special choice of intensity distributions, ν does not depend on μ_x. This is not essential, however, except it simplifies formulas.

Using this in conjunction with equation (S15) allows analytical calculation of the ML estimator for μ_x,

$$\hat{\mu}_x = \frac{\lambda}{4\pi}\arccos\left(\frac{N_1 - N_2}{N_1 + N_2}\right)\ . \tag{S24}$$

Its bias and variance may be found readily:

$$\begin{aligned} \langle\hat{\mu}_x\rangle &= \mu_x - \frac{\lambda}{16\pi}\frac{\nu_1 - \nu_2}{(\nu_1 + \nu_2)\sqrt{\nu_1\nu_2}}\ , && \text{(S25)} \\ \mathrm{Var}(\hat{\mu}_x) &= \frac{\lambda^2}{16\pi^2}\frac{1}{\nu}\ . && \text{(S26)} \end{aligned}$$

Note that the bias vanishes where the two expected photon counts are equal, as it must for symmetry reasons. Note also that the bias diverges if one of the expected photon counts goes to zero, but vanishes if one of the expected photon counts is exactly zero. The standard deviation does not depend on μ_x, since ν does not. It agrees with the result in Balzarotti et al., equation (S22h). For comparison, if λ is identical to the wavelength of the the emitted light, the spatial s.d. of a Gaussian PSF is roughly $\sigma_{\mathrm{PSF}} = \lambda/(4\mathrm{NA}) = \lambda/6$ for a numerical aperture of NA = 1.5. In the absence of fluorescent background and with infinitely small pixels, the variance of such camera-based localization is $\mathrm{Var}(\mu_x) = \lambda^2/36\nu$. Thus, in this idealised 1D case, the photon efficiency of camera-based MINFLUX is a factor of ~ 4 better than camera-based localization. Similar considerations lead to a possible factor improvement of ~ 2.5 in 2D. If the wavelength of the structured illumination were reduced to 300 nm, e.g., the possible improvement factor instead would be ~ 4.5 in 2D (**Fig. 1c** and **Supplementary**

Fig. 1). If instead, the wavelength were 600 nm, the improvement factor would be ~ 1.7 in 2D. Note again that the benefits of whole-FOV throughput of camera-based MINFLUX analysis comes about only through the combination with camera-based localization, since camera-based MINFLUX only determines the position of the point-source *relative* to *a period* of the periodically structured illumination.

Supplementary Note 7: C-MELM theory

As described in the main text, C-MELM simultaneously extracts information from the number of detected source photons under multiple known structured illuminations and from the spatial distributions of those photons in images. For each point-source, C-MELM takes as input N_{images} images of spots that have been acquired under illumination structures that are known mathematically. Consider initially a set of illumination structures with structure along the x-axis only, as in equations (S11) and (S12). Since the illumination varies along the x-axis only, the expected number of photons from the source depends on μ_x but not on μ_y. Specifically, in the j'th image,

$$\nu_j(\mu_x) = I f(\mu_x + \phi_j) \ , \tag{S27}$$

where ϕ_j is the corresponding phase-shift of the structured illumination. The sum of expected total number of photons recorded from the point-source in all images is

$$\nu = I \sum_{j=1}^{N_{\text{images}}} f(\mu_x + \phi_j) \ . \tag{S28}$$

In practice, as depicted in **Figs. 2** and **4**, we will use the *relative* number of total source photons detected during a given image under structured illumination,

$$r_j(\mu_x) = \frac{\nu_j(\mu_x)}{\nu} \ , \tag{S29}$$

which is independent of I. This highlights that a characterization of the illumination structure obtained, e.g., with fluorescent beads may be used also for C-MELM measurements of positions of other point-sources. The camera-based imaging, additionally, gives access to the spatial distribution of the detected photons, which, in principle, allows direct determination of the point-source's position by fitting of a theoretical PSF. Here, we combine such PSF-fitting and camera-based MINFLUX. To do so, we will apply a joint MLE fit of a PSF model to spots produced by the point-source in all images.

As a model for the PSF, we will use the 2D-Gaussian-plus-a-constant described above. In all images, $\vec{\mu}$ and σ^2_{PSF} are constant. The normalization constant of the Gaussian part of the PSF, on the other hand, depends on the intensity of structured illumination at the position of the point-source. Since this normalization constant, $\langle N_j \rangle$, is proportional to the total number of source photons, ν_j, the relative photon number observed in the j'th image may also be written as

$$r_j(\mu_x) = \frac{\langle N_j(\mu_x) \rangle}{\langle N \rangle} \ . \tag{S30}$$

In terms of r_j, the normalization constant of the Gaussian PSF in image j is thus $\langle N_j(\mu_x) \rangle = r_j(\mu_x)\langle N \rangle$.

As discussed above, with this PSF model, the "background" includes a contribution from the slowly decaying tails of the actual PSF. The expected value of this contribution, $\langle b^2_{\mathrm{PSF}}\rangle$, also is proportional to the structured illumination at the point-source's position. Thus, $\langle b^2_{\mathrm{PSF},j}\rangle = \langle b^2_{\mathrm{PSF}}\rangle r_j(\mu_x)\langle N\rangle$, which varies as a function of image number j but is effectively constant in the vicinity of the point-source. We found that the part of this background in the region of interest around a spot amounts to 20 per cent relative to the source photons comprising the Gaussian peak of the PSF. The expected value of the remaining contribution to the "background", $\langle b^2_{\mathrm{actual}}\rangle$, is due to actual background, which we assume independent of excitation intensity and thus constant from image to image.

In the joint MLE fit, we constrain the normalization constant of each Gaussian and the PSF-derived contribution to the "background" in each image to the value expected from the characterization of the structured illumination. With this choice, the expected number of photons in pixel number i in image number j is

$$\begin{aligned} E_{i,j} &= \langle N_j(\mu_x)\rangle\, p_i(\vec{\mu}) + \langle b^2_{\mathrm{PSF},j}\rangle + \langle b^2_{\mathrm{actual}}\rangle \\ &= \langle N\rangle r_j(\mu_x) p_i(\vec{\mu}) + \langle b^2_{\mathrm{PSF}}\rangle\langle N\rangle\, r_j(\mu_x) + \langle b^2_{\mathrm{actual}}\rangle \ , \end{aligned} \tag{S31}$$

where p_i is given by equation (S1). Note that $E_{i,j}$ is a function of both position coordinates, $\vec{\mu} = (\mu_x, \mu_y)$, since p_j is, but of μ_x alone through $\langle N_j\rangle$ and $\langle b^2_{\mathrm{PSF},j}\rangle$. We are left with six parameters to be determined from the N_{images} images of a spot, i.e. $\theta = \{\vec{\mu}, \sigma^2_{\mathrm{PSF}}, \langle N\rangle, \langle b^2_{\mathrm{PSF}}\rangle, \langle b^2_{\mathrm{actual}}\rangle\}$. The log-likelihood function is

$$\ell = \sum_{j=1}^{N_{\mathrm{images}}} \sum_{i=1}^{N_{\mathrm{pixels}}} \left[-E_{i,j} + n_{i,j}\log E_{i,j}\right] \ , \tag{S32}$$

where $n_{i,j}$ is the number of photons detected in the i'th pixel in the j'th image. In order to obtain the C-MELM estimates for the parameters, this log-likelihood function is maximized numerically with respect to θ.

In the above, we restricted the illumination to contain structure along the x-axis only. Consequently, only the precision of μ_x, and not of μ_y, is enhanced relative to camera-based localization based on the same images. To extend this analysis to 2D, images with structure along the y-axis must be acquired as well. Consider now the case where images have been acquired with structure along each axis. While all images, regardless of illumination structure, contain information about the point-source's position through the $\vec{\mu}$-dependence of p_j, only images with structure along a certain axis improve the precision of that coordinate. Therefore, we separately consider the relative photon numbers detected from the point-source during exposures to structured illumination along each of the axes. The relative photon numbers now depend on the direction of structure in images, and, effectively, replace equation (S30) with a relative photon number corresponding to images with structure along the x-axis, $r_j^{(x)}(\mu_x) = \langle N_j^{(x)}(\mu_x)\rangle / \langle N^{(x)}\rangle$, and the y-axis, $r_j^{(y)}(\mu_y) = \langle N_j^{(y)}(\mu_y)\rangle / \langle N^{(y)}\rangle$. With this, C-MELM analysis in 2D amounts to maximization w.r.t. $\theta = \{\vec{\mu}, \sigma^2_{\mathrm{PSF}}, \langle N^{(x)}\rangle, \langle N^{(y)}\rangle, \langle b^2_{\mathrm{PSF}}\rangle, \langle b^2_{\mathrm{actual}}\rangle\}$ of

$$E^{(x)}_{i,j} = \langle N^{(x)}\rangle r_j(\mu_x) p_i(\vec{\mu}) + \langle b^2_{\mathrm{PSF}}\rangle\langle N^{(x)}\rangle\, r_j(\mu_x) + \langle b^2_{\mathrm{actual}}\rangle \ , \tag{S33}$$

$$E^{(y)}_{i,j} = \langle N^{(y)}\rangle r_j(\mu_y) p_i(\vec{\mu}) + \langle b^2_{\mathrm{PSF}}\rangle\langle N^{(y)}\rangle\, r_j(\mu_y) + \langle b^2_{\mathrm{actual}}\rangle \ , \tag{S34}$$

respectively, for images obtained with x-periodic and y-periodic illumination structures.

Supplementary Note 8: Variance of C-MELM estimates

The elements of the Fisher information matrix are defined as [9]

$$I(\theta)_{p,q} = -\left\langle \left(\frac{\partial l}{\partial \theta_p} \frac{\partial l}{\partial \theta_q} \right) \right\rangle \quad , \tag{S35}$$

where ℓ is the log-likelihood function given in equation (S32), and θ_p and θ_q are components of the parameter set θ.

Partial differentiation of the log-likelihood function with respect to any parameter θ_k yields

$$\frac{\partial \ell}{\partial \theta_k} = \sum_{j=1}^{N_{\text{images}}} \sum_{i=1}^{N_{\text{pixels}}} \left[-\frac{\partial E_{i,j}}{\partial \theta_k} + n_{i,j} \frac{1}{E_{i,j}} \frac{\partial E_{i,j}}{\partial \theta_k} \right] \quad . \tag{S36}$$

With some algebra and utilization of the fact that all images and pixels are independent, it can be shown that the general Fisher information matrix elements can be written as

$$I(\theta)_{p,q} = -\left\langle \left(\frac{\partial l}{\partial \theta_p} \frac{\partial l}{\partial \theta_q} \right) \right\rangle = \sum_{j=1}^{N_{\text{images}}} \sum_{i=1}^{N_{\text{pixels}}} \frac{1}{E_{i,j}} \frac{\partial E_{i,j}}{\partial \theta_p} \frac{\partial E_{i,j}}{\partial \theta_q} \quad . \tag{S37}$$

The Fisher information matrix can be evaluated numerically by calculating the elements as above. Note that aside from assuming Poisson-distributed photon counts in each pixel, no further assumptions have been made, e.g., in regards to the dimensionality of the image or the specific functional form of $E_{i,j}$. The above expression thereby applies to both 1D and 2D images with any choice of illumination structures.

In the case of C-MELM, seven parameters are estimated: $\theta = \{\vec{\mu}, \sigma^2_{\text{PSF}}, \langle N^{(x)} \rangle, \langle N^{(y)} \rangle, \langle b^2_{\text{PSF}} \rangle, \langle b^2_{\text{actual}} \rangle\}$, which makes the Fisher information matrix a 7×7 matrix. The covariance matrix for a C-MELM estimate is $\text{Cov}(\theta) = I^{-1}(\theta)$. The minimal attainable variance of such a parameter, its Cramér-Rao lower bound, may be found as the corresponding diagonal element in the covariance matrix. Whenever we discuss theoretical variances of C-MELM, we refer to these bounds.

Supplementary Note 9: Modelling of the non-harmonic illumination structure

In order to use the DMD-generated structured illumination resulting from three-beam-interference for C-MELM, it must be characterised mathematically. Basically, each of the micrometer-sized quadratic mirrors in the array can be either "on" (reflection of light to sample) or "off" (reflection away from sample). For 1D-periodic configurations of mirrors, as considered in this work, the individual mirror configuration is described by its duty cycle d/c, where d is the number of "on" mirrors per period, and c is the number of total mirrors per period. In this work, we used $d/c = 1/8$ (Methods, **Supplementary Figs. 7** and **11**).

In 1D, we model the binary state of the DMD array as a function M of distance x in the sample plane as a piecewise constant function taking values of either 1 ("on") or 0 ("off"). Thus,

$$M(x) = \sum_{n=0}^{N_{\text{periods}}/2} H\left(-x + \frac{dw}{2} \pm ncw\right) H\left(x + \frac{dw}{2} \mp ncw\right) \quad , \tag{S38}$$

where N_{periods} is the total number of mirror periods, H is the Heaviside step function, and w the effective width of a single mirror (**Supplementary Fig. 7c**).

Before illumination of the sample, this structured illumination is subject to diffraction as it passes through the objective lens. Since the structure is confined to 1D, we account for diffraction by a convolution with a 1D-Gaussian PSF of width σ_{SI},

$$G(x) = \frac{1}{\sqrt{2\pi\sigma_{\text{SI}}^2}} \exp\left(-\frac{x^2}{2\sigma_{\text{SI}}^2}\right) \quad . \tag{S39}$$

The resulting illumination structure in the sample plane is

$$P(x) = A(M * G)(x) + B \enspace , \tag{S40}$$

where A is the amplitude of the structured illumination and B is a constant background (**Supplementary Fig. 7d**). The latter term accounts also for contributions to the illumination structure from the slowly decaying tails of the actual PSFs, which we have disregarded by assuming a Gaussian PSF model. This approximation, however, is sufficiently accurate for our purposes, as discussed in the main text.

The convolution $(M * G)(x)$ can be exactly evaluated as a sum of error functions,

$$(M * G)(x) = \frac{1}{2} \sum_{n=0}^{N_{\text{periods}}/2} \left(\operatorname{erf}\left(\frac{x + \frac{dw}{2} \mp ncw}{\sqrt{2\sigma_{\text{SI}}^2}}\right) + \operatorname{erf}\left(\frac{-x + \frac{dw}{2} \pm ncw}{\sqrt{2\sigma_{\text{SI}}^2}}\right)\right) \quad . \tag{S41}$$

For fitting purposes, N_{periods} should be chosen sufficiently large for the PSF to have vanished.

Alternatively, the convolution can be approximated in a series expansion, as described in [3],

$$(M * G)(x) \approx \frac{1}{c} \int_0^d \left(1 + 2\sum_{k=1}^{K} \exp\left(-2k^2\left(\frac{\pi\sigma_{\text{SI}}}{cw}\right)^2\right) \cos\left(\frac{2k\pi}{cw}(s - x)\right)\right) ds \enspace , \tag{S42}$$

where K is the number of terms included in the series expansion. For all investigated parameter values, $K = 3$ was sufficient to accurately describe the convolution, i.e. yielding indistinguishable results to the exact convolution in equation (S41), along with a small benefit in terms of computational speed.

Regardless of the choice of convolution representation, a weighted least-squares approach was used to determine the parameters describing the illumination structure $(A, B, w, \sigma_{\text{SI}}, \phi)$, where ϕ denotes a phase shift of the illumination structure relative to the origin of the axis. Common values for parameters (w, σ_{SI}) in our non-harmonic SI experiments were $w \approx 51$ nm and $\sigma_{\text{SI}} \approx 64$ nm, respectively.

Supplementary Note 10: Interpolation between illumination structures

In order to apply C-MELM, one must know the realized illumination structure near the position of the point-source. We obtained such characterizations only at the random positions of immobilized fluorescent beads serving as fiducials, which, typically, do not co-localize with a point-source of interest. Instead, we interpolate between such characterizations.

The camera-based imaging allows a crude localization of the point-source in the field-of-view (**Fig. 4**). Following this, the $N_{\text{fiducials}}$ nearest characterizations of illumination structures $P_{i=1,\ldots,N_{\text{fiducials}}}$ were combined to yield a local representation of the illumination structure. For the results obtained in the present work, $N_{\text{fiducials}} = 5$ was used.

To obtain the interpolation, initially, we averaged each of the parameters, A_i, B_i, w_i, and $\sigma_{\text{SI},i}$, using the distance from the fiducial to the point-source of interest as weight.

To determine the phase shift of the interpolated illumination structure, we extrapolated all $N_{\text{fiducials}}$ characterizations for a single phase of the structured illumination along each axis. Then, we considered those extrapolations near the crudely localized position of the point-source of interest (**Supplementary Figure 13** illustrates this for a single coordinate).

For these $N_{\text{fiducials}}$ extrapolated illumination structures, the intensity peak closest to the position of the point-source was determined for each orientation of the structured illumination - this served as a prediction of the peak position if each illumination structure were extrapolated individually. Due to slow variations of the illumination structure over the FOV, the extrapolated peak positions p_x and p_y for each of the $N_{\text{fiducials}}$ illumination structures varied approximately linearly with extrapolation distance to the point-source. The main contribution is from a slight rotation of the lines in the structured illumination relative to the image axes. We thus have

$$p_x = a_x x_{\text{ext}} + b_x y_{\text{ext}} + k_x \tag{S43}$$

$$p_y = a_y x_{\text{ext}} + b_y y_{\text{ext}} + k_y \tag{S44}$$

Note here that x_{ext} and y_{ext} are the extrapolated x- and y-distances of the characterized illumination structures, respectively. The parameters $(a_x, b_x, a_y, b_y, k_x, k_y)$ were obtained by a least-squares fit to data. The estimated peak position of, e.g., the interpolated x-periodic illumination structure was extracted as $p_x(x_{\text{ext}} = y_{\text{ext}} = 0) = k_x$. The phase shift $\phi_{\text{int},x}$ was calculated as

$$\phi_{\text{int},x} = \text{mod}(p_x - \bar{w}/2, 8\bar{w}) \tag{S45}$$

where mod is the modulo function and bar implies a weighted average.

The interpolated illumination structure is

$$P_{\text{interpolated}} = P(\bar{A}, \bar{B}, \bar{w}, \bar{\sigma}_{\text{PSF}}, \phi_{int}) \ . \tag{S46}$$

Supplementary Note 11: Illumination structure impact on C-MELM precision

Obviously, the amount of information available to C-MELM depends on the realised structure. In particular, the illumination structure's *period* and *contrast* are important. We define the contrast as

$$C = \frac{P_{\max} - P_{\min}}{P_{\max} + P_{\min}} \ , \tag{S47}$$

which takes a value between 0 and 1. Note that ideal contrast of 1 is achieved only for $P_{\min} = 0$, which seems hard to realise with a DMD-based solution.

Shorter period and/or higher contrast result in an increase of the intensity profile's gradient, in larger differences in relative photon numbers between exposures, and thus in increased information about the point-source's position. However, shorter period and higher contrast are generally mutually exclusive when using the maximally simple three-beam interference DMD setup depicted in **Supplementary Figure 5** (**Supplementary Fig. 11**). Reducing the period below a certain limit has a negative impact on the contrast as a result of diffraction—if the on-mirror reflection intensities are too close to each other, the resulting diffraction will result in an overlap of neighbouring peaks, producing a low-contrast illumination structure and thus poor resolution (**Supplementary Fig. 11a**). Conversely, increasing the period has a positive impact on contrast, but increasing it too much produces illumination structures with large areas of no intensity gradients (**Supplementary Fig. 11b**). This thus indicates that in terms of information extraction from the structured illumination, an optimal choice of duty cycle exist, which provides a high contrast at the shortest possible period (**Supplementary Fig. 11c**). In our experiments we used a duty cycle of 1/8.

The relative performance of C-MELM and conventional camera-based localization microscopy may be evaluated numerically by comparison of their theoretical variances, i.e. their CRLB, for estimated position coordinates.

The relative performance for various values of the period and contrast can be evaluated by comparing the CRLB of camera-based localization and C-MELM, calculated from equation (S37). The results are shown in **Supplementary Figure 11d**.

Supplementary Figures

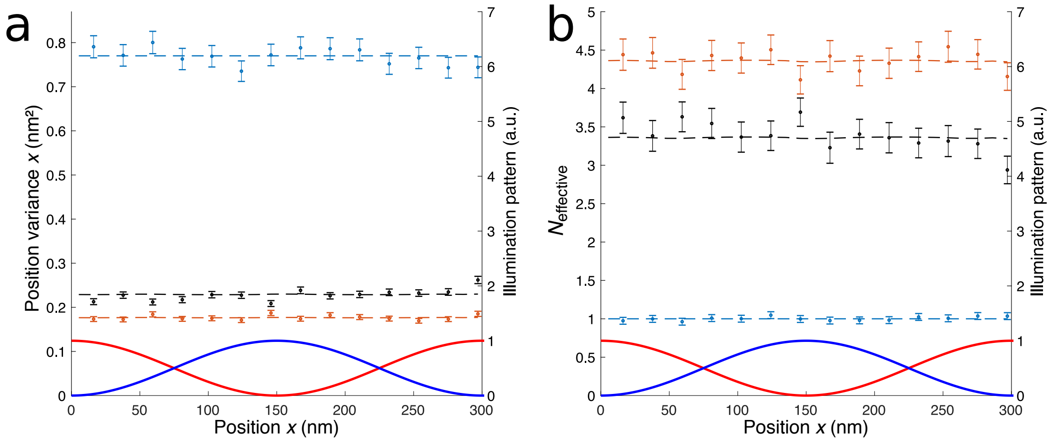

Supplementary Figure 1. Simulation: Performance of maximally simple implementation of C-MELM. Four images (two for each of two orthogonal directions) per "frame" of a simplified 2D C-MELM experiment (2D-extension of Fig. 1**a**,**b**) were Monte Carlo simulated 2,000 times for different positions of a particle relative to the harmonic structured illumination (red and blue curves, right y-axis). We assumed a pixel size of 108 nm and a known structured illumination with an ideal contrast of 1 and a period of 300 nm. We used Poisson statistics for the photons detected with each pixel in each image. (**a**) The variance of estimates for one coordinate of the particle's location was calculated for each position of the particle relative to the structured illumination, showing a significant reduction in variance for C-MELM (red data points, left y-axis) and camera-based MINFLUX (black data points, left y-axis) compared to PSF-fitting (blue data points, left y-axis). Each method achieves its respective Cramér-Rao lower bound (CRLB, dashed lines). Error bars represent s.d. of the sample variance. (**b**) Same data as **a**, here plotted in terms of $N_{\text{effective}}$ instead (see equation 1 in the main paper). For all particle positions, C-MELM achieves a value for $N_{\text{effective}}$ that is a factor of ~ 4.4 better than PSF-fitting (**Fig. 1c**) and a factor of ~ 1.3 better than camera-based MINFLUX with the same SIs. This improvement in $N_{\text{effective}}$ is comparable to the value that we realised experimentally with a harmonic illumination structure (**Fig. 3**). Error bars represent standard error of the calculated $N_{\text{effective}}$.

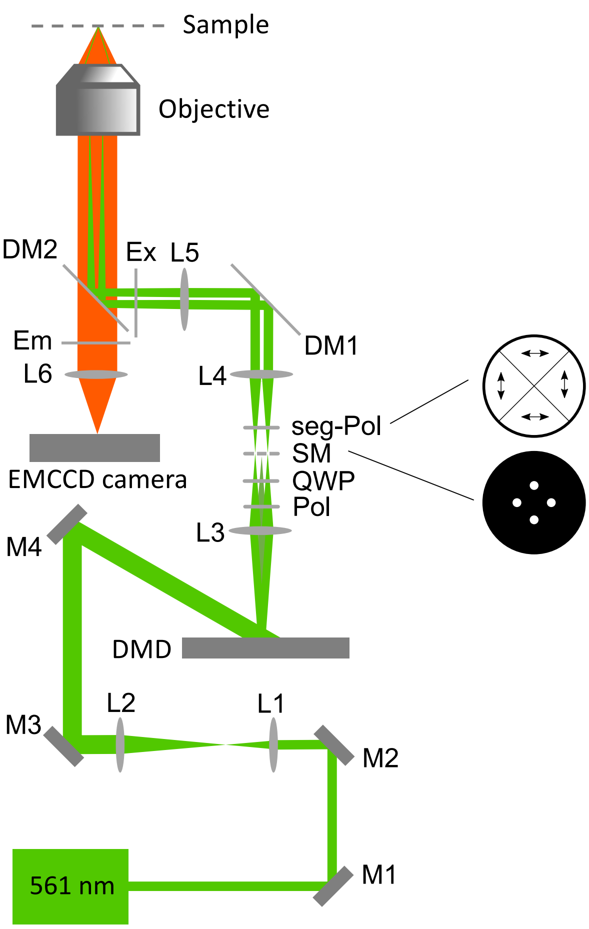

Supplementary Figure 2. Full schematic of the experimental setup. Extended version of **Figure 2a**. The 561 nm laser was guided through a polarizing beam splitter (PBS) to reduce the power. The beam was guided by mirrors (M1 and M2) to a telescope set-up (L1 and L2), causing a beam expansion. The beam was then guided by mirrors (M3, M4) to the DMD. They were adjusted to ensure that the beam reflection off "on"-mirrors was normal to the DMD. The beam from the DMD was focused through a pair of identical lenses (L3 and L4) followed by a dichroic mirror and a lens L5 before it is guided by the dichroic mirror of the filter cube assembly (DM2) through the objective and onto the sample. The filter cube assembly also includes an excitation filter (Ex). The $4f$ configuration of L3, L4, L5 and the objective ensured that the back focal plan of the objective is accessible in a conjugated plan at the focus of the telescope formed by L3 and L4. In the focal plane we place a home-made spatial mask (SM, bottom inset) and segmented polarizer (seg-Pol, top inset) to remove the zeroth order diffraction of the line pattern displayed on the DMD and ensure the linear polarization of the first diffraction order spots send to the objective. This, together with the polarizer and the quarter wave plate (QWP) placed after the DMD ensured that the intensity of the pattern is almost constant for both direction of lines displayed on the DMD. The emission of the sample was guided back through the objective, emission filter (Em), and tube lens (L6) to be recorded on an EMCCD camera.

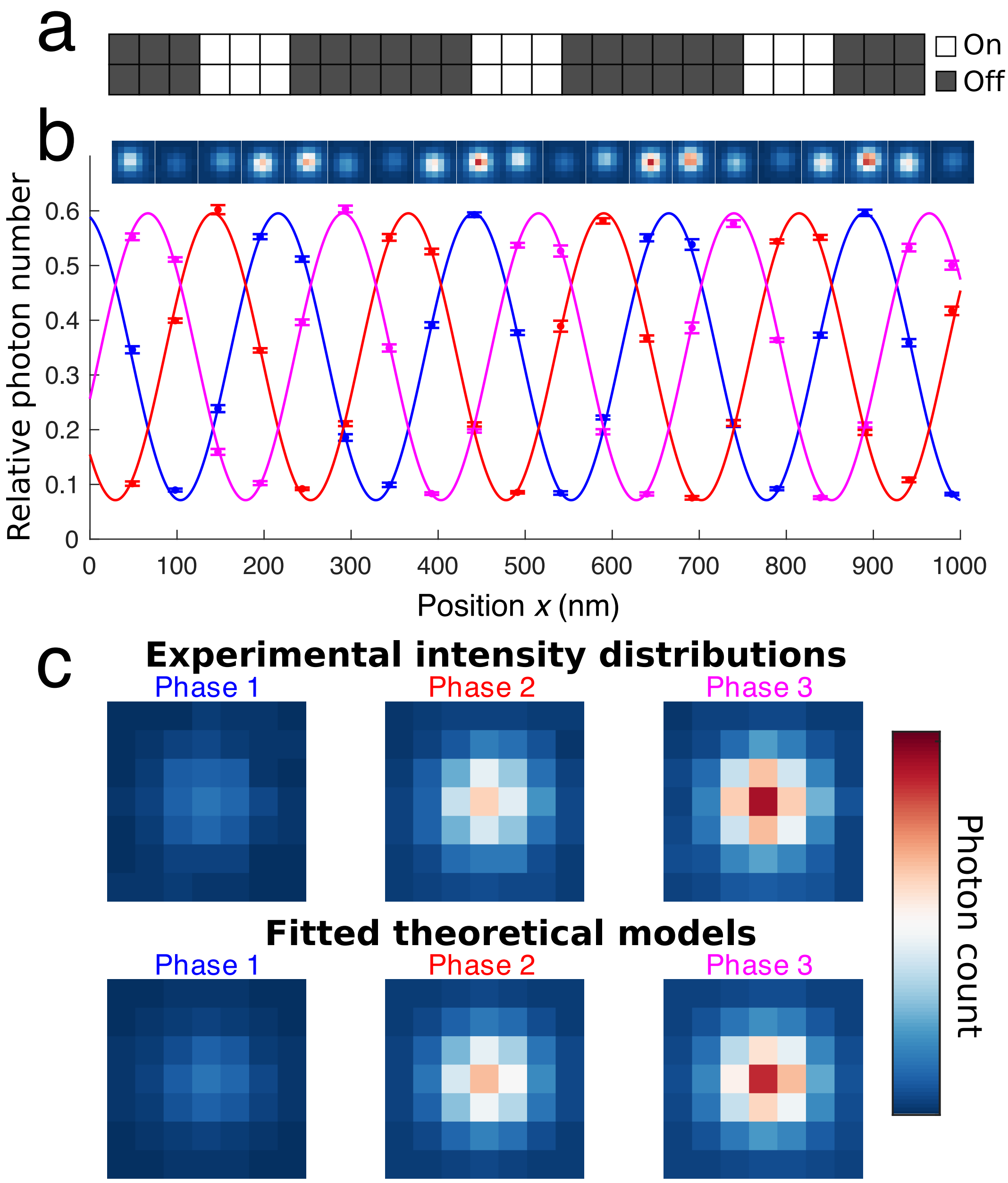

Supplementary Figure 3. Characterization of the x-periodic harmonic illumination structure. These results use the same bead and approach as shown in **Figure 2 b–d**.

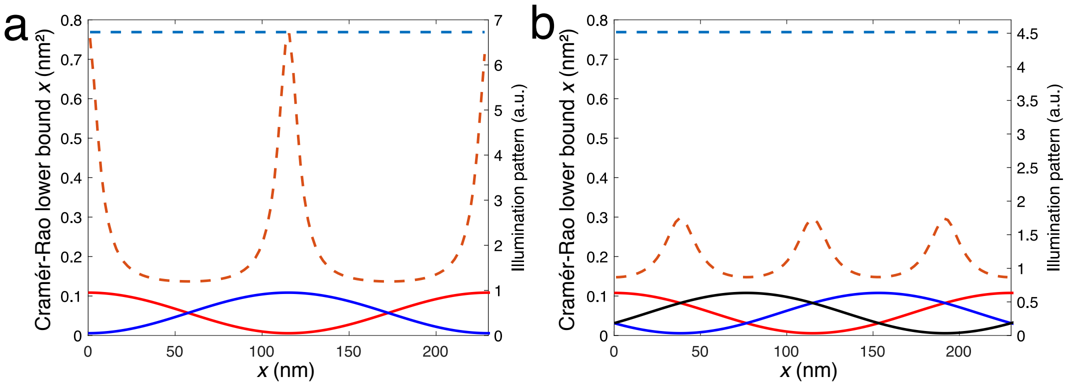

Supplementary Figure 4. Dependency of C-MELM CRLB on particle position relative to the SI using harmonic illumination profiles. (**a**) Comparison of Cramér-Rao lower bounds (CRLBs) for one position coordinate for, respectively, optimal fitting of PSFs (blue dashed line, left y-axis) and C-MELM (red dashed line, left y-axis) as a function of the particle's position relative to the structured illumination. As the structured illumination is perfectly harmonic, the total photon count remains constant at all positions. Two images (phases) of our experimentally realized harmonic structured illumination (along each axis) shifted half a period relative to each other (red and blue solid curves, right y-axis). While the CRLB for PSF-fitting remains constant, the CRLB for C-MELM varies significantly with position. C-MELM's improvement in localization is maximal where the gradients of the SIs are large (equal intensities of the SIs), while improvements are negligible in the region with small gradients (near extremums of the SIs). (**b**) Same as **a** assuming three phases of the harmonic structured illumination (along each axis) shifted a third of a period relative to each other (red, blue, black solid curves, right y-axis). The CRLB for C-MELM varies significantly less than when using two images as in **a**.

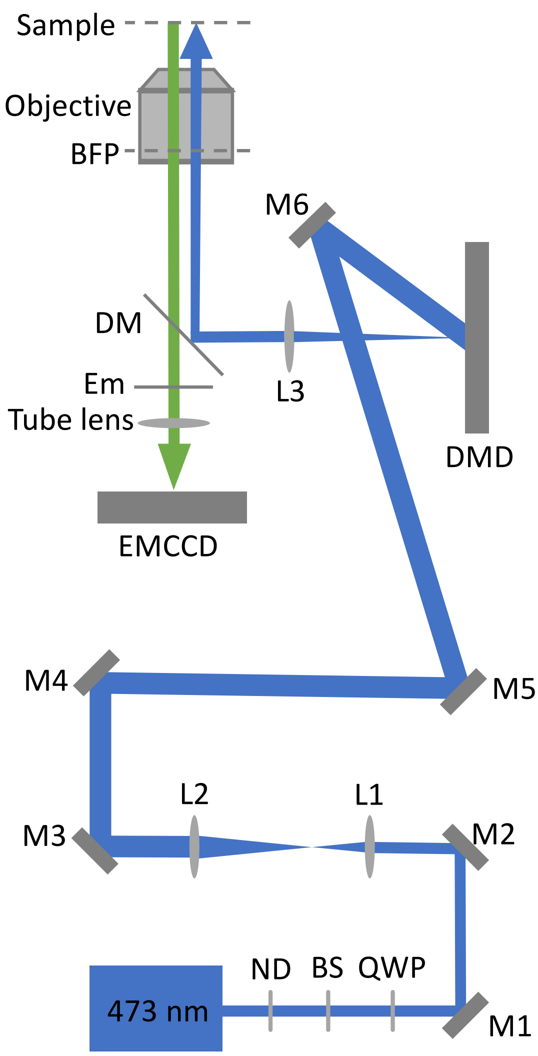

Supplementary Figure 5. Full schematic of the alternative setup for widefield SI. The 473 nm laser was guided through a neutral density filter (ND), a polarizing beam splitter (PBS), and a quarter wave plate (QWP) to reduce the power of the laser and to create circularly polarized light. The beam was guided by mirrors (M1 and M2) to a telescope set-up (L1 and L2), causing a beam expansion. The beam was then guided by mirrors (M3, M4, M5 and M6) to the DMD. They were adjusted to ensure that the beam reflection off "on"-mirrors was normal to the DMD. The beam from the DMD was focused through a lens (L3) and guided by the dichroic mirror (DM) through the objective and onto the sample in a $4f$ configuration. The emission of the sample was guided back through the objective, emission filter (Em), and tube lens to be recorded on an EMCCD camera.

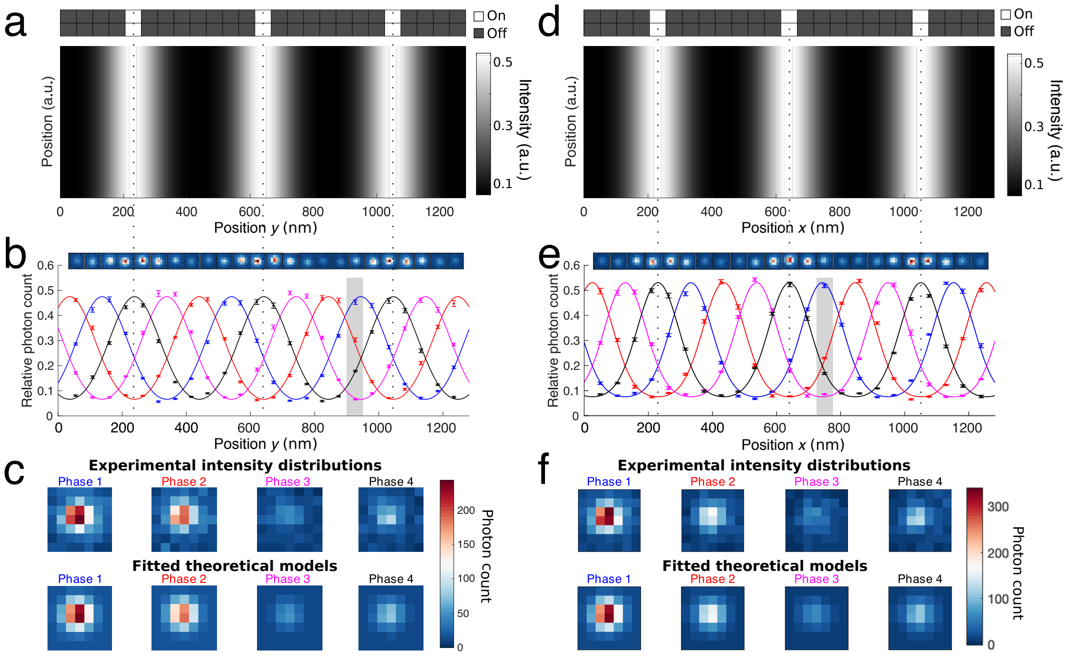

Supplementary Figure 6. Characterization of the non-harmonic illumination structure. (**a**) Subset of the DMD array configured in a periodic series of "on" and "off"-mirrors (top) and the resulting 1D y-periodic SI at the sample plane (bottom). The intensity peaks of the SI coincide with the center position of the "on"-mirrors. (**b–c**) Example characterization of the non-harmonic SI, similar in approach to that of **Figure 2**, however using a single 51-nm fluorescent bead instead. (**b**) Estimated relative intensity as a function of position for the non-harmonic SI, obtained similarly to description in **Figure 2**. As the SI was non-harmonic, we used a diffraction model with parameters obtained by a fit to data (colored curves) that describes the data perfectly and thus characterizes the SI. Error bars represent standard error of the calculated relative photon numbers. (**c**) Experimental bead images (top row) obtained at a single stage position (gray area in **b**) under illumination from four different phases as in **b**. All four images are fitted with a PSF (bottom row) for a point-source under assumption that its position is identical in the four images. This enables accurate estimation of total intensity also in dim images (e.g. for Phase 3). (**d–f**) Same as **a–c** for the x-periodic illumination using the same bead.

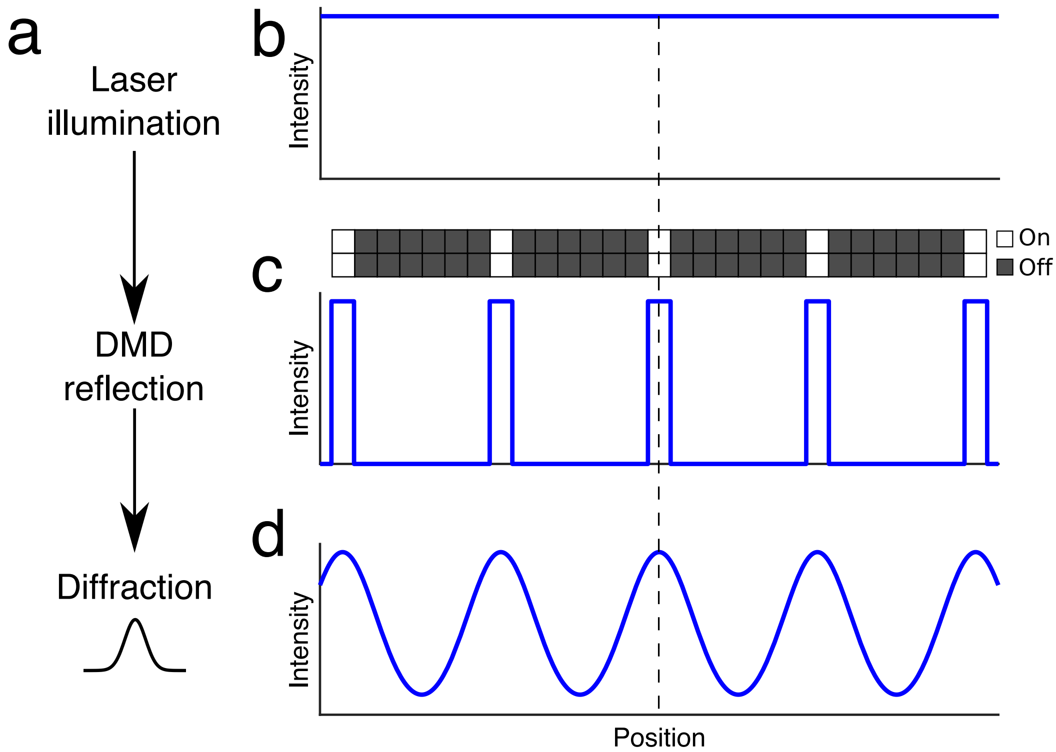

Supplementary Figure 7. Simple theoretical model of formation of structured illumination using a DMD in a three-beam interference setup. (**a**) Simplified schematic of illumination pathway from laser to sample plane, consisting of the laser illumination being reflected off the DMD before diffraction at objective. (**b**) We model the laser illumination as a field of uniform intensity for all positions of interest. (**c**) The uniform illumination is reflected off the DMD, which is configured so that only light reflected off "on" mirrors (white) reaches the sample. This results in an intensity comprised of a series of top-hat functions (equation (S38)). All mirrors are of identical effective width w. (**d**) The top-hat intensity profile is focused through the objective, where it is subject to diffraction, which we model as a convolution (equation (S40)) of the incident intensity profile and a Gaussian PSF of width σ_{SI} (equation (S39)). For the specific choice of mirror configuration shown here ($d/c = 1/7$), the resulting theoretical illumination structure is near-harmonic with contrast $C \approx 0.8$.

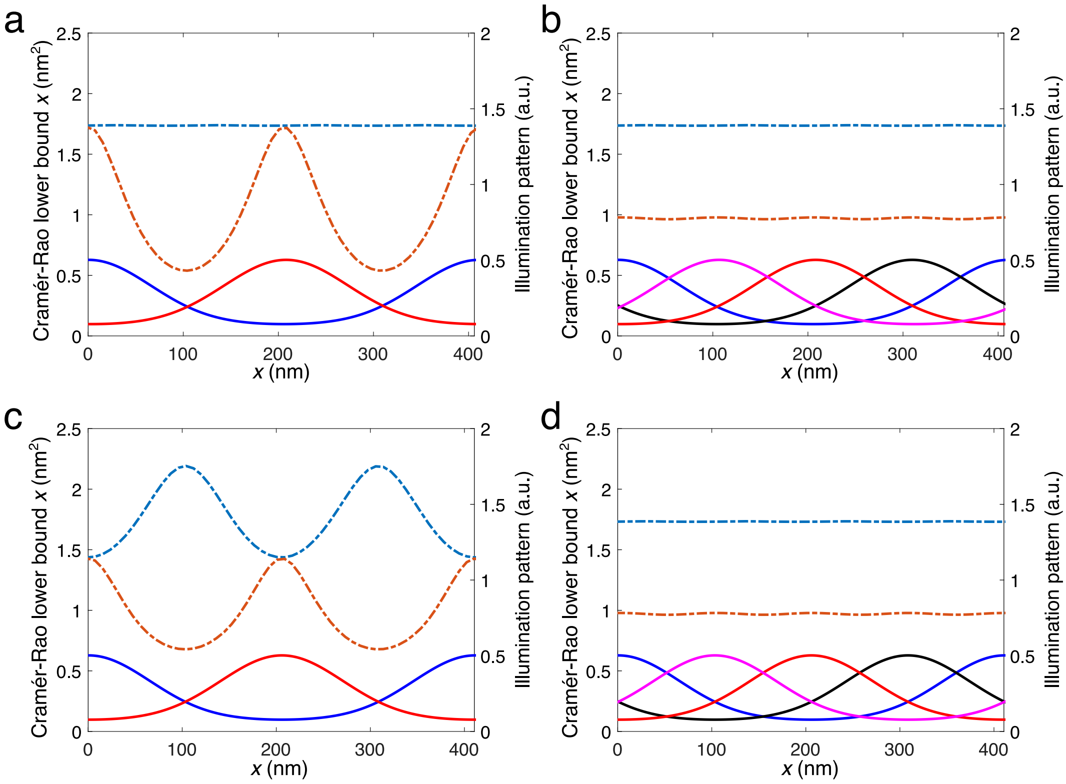

Supplementary Figure 8. Dependency of C-MELM CRLB on particle position relative to the SI using non-harmonic illumination profiles. (**a**) Comparison of Cramér-Rao lower bounds (CRLBs) for one position coordinate for, respectively, optimal fitting of PSFs (blue dashed line, left y-axis) and C-MELM (red dashed line, left y-axis) as a function of the particle's position relative to the structured illumination. Here we assumed constant total photon count, and two images (phases) of our experimentally realized non-harmonic structured illumination (along each axis) shifted half a period relative to each other (red and blue solid curves, right y-axis). While the CRLB for PSF-fitting remains constant, the CRLB for C-MELM varies significantly with position. C-MELM's improvement in localization is maximal where the gradients of the SIs are large (equal intensities of the SIs), while improvements are negligible in the region with small gradients (near extremums of the SIs). (**b**) Same as **a** assuming four phases of structured illumination (along each axis) shifted a quarter period relative to each other (red, blue, black, and magenta solid curves, right y-axis). The CRLB for C-MELM remains within 1% of its average value, which provides close to uniform improvement of localization. (**c**) Same as **a** under assumption of constant exposure time at all particle positions relative to the SI. Due to the non-harmonic structured illumination, the total photon number varies with particle position. This causes the CRLB for PSF-fitting to also vary with particle position. (**d**) Same as **b** under the assumptions described in **c**. The CRLB for both methods remain within 1% of their respective average values.

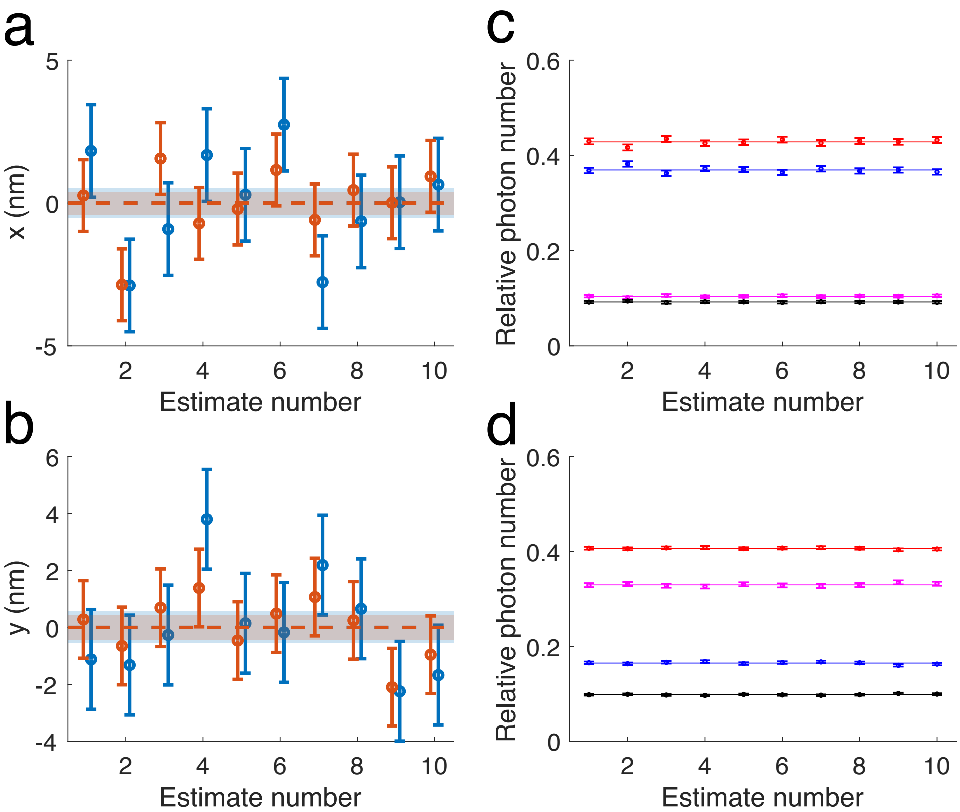

Supplementary Figure 9. Individual estimates and consistency check of demonstration C-MELM measurements. Extension of data from **Figure 4**. (**a,b**) 2D position estimates, x (**a**) and y (**b**), obtained in ten repeated applications of C-MELM (black) and optimal fitting of PSFs (red) on the bead shown in Fig. 4A. Error bars indicate theoretical s.d. (Methods). The weighted average positions are indicated and indistinguishable for the two methods (dashed lines, shaded areas represent s.e.m.). Notice the tighter scatter of the C-MELM estimates around the average position, consistent with their smaller theoretical error bars. (**c,d**) Ten estimates of the relative photon number in each spot for each phase of the x-periodic (**c**) and y-periodic (**d**) illumination as obtained implicitly with C-MELM (dots with color coding identical to that of **Figure 4c,d**). The average relative photon numbers are indicated (solid lines). Error bars represent theoretical s.d. (Methods).

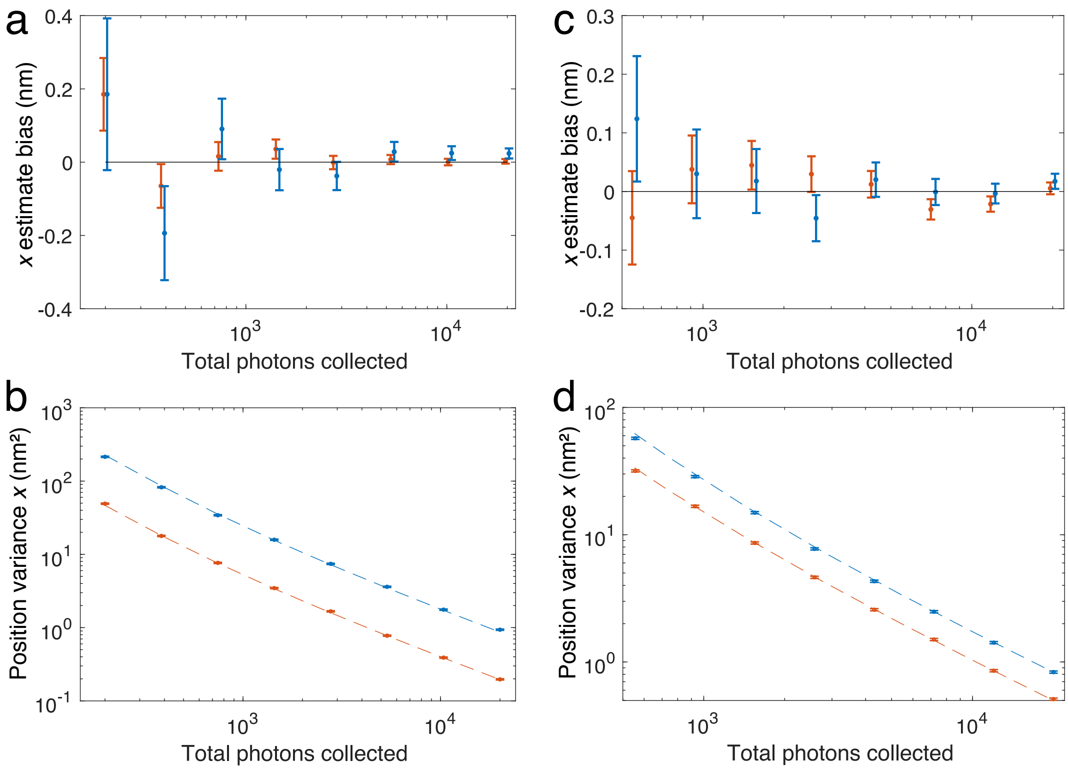

Supplementary Figure 10. Simulation: Precision and accuracy of C-MELM. Monte Carlo simulation study of 2D C-MELM precision for varying total photons collected, using three phases of harmonic illumination profiles (**a,b**) and four phases of non-harmonic illumination profiles (**c,d**) along each axis. Six/eight images per "frame" of a 2D C-MELM experiment were Monte Carlo simulated 5,000 times for different total photon numbers. For the simulations, we used parameters values that corresponded to our experiments. Specifically, we used a pixel size of 108 nm, along with an SI contrast of 0.9 and a period of 230 nm in the harmonic case (**a,b**), and a contrast of 0.76 and period of 406 nm in the non-harmonic case (**c,d**). We assumed Poisson statistics for the number of photons detected in each pixel of each image. The images of each "frame" were analyzed with C-MELM in a manner identical to the analysis of our experimental data (Methods). (**a**) Average deviation of estimates of the particle's x-coordinate from its true value, i.e. bias, for, respectively, PSF-fitting (blue) and C-MELM (red) using harmonic illumination profiles. Error bars represent s.e.m.. Both methods are accurate, i.e. unbiased, for all considered values of total photons. (**b**) Variance of estimates of the particle's x-coordinate using the same simulated data as in **a**. The respective Cramér-Rao lower bound (CRLB) for each method is indicated (dashed lines). For all considered total photon numbers, both methods are maximally precise in the sense that they achieve their respective CRLB. (**c**) Same as **a**, using non-harmonic illumination profiles. Both methods are accurate for all considered values of total photons. Error bars represent s.d. of the sample variance. (**d**) Same as **b**, using non-harmonic illumination profiles. Both methods are maximally precise, as they achieve their respective CRLB.

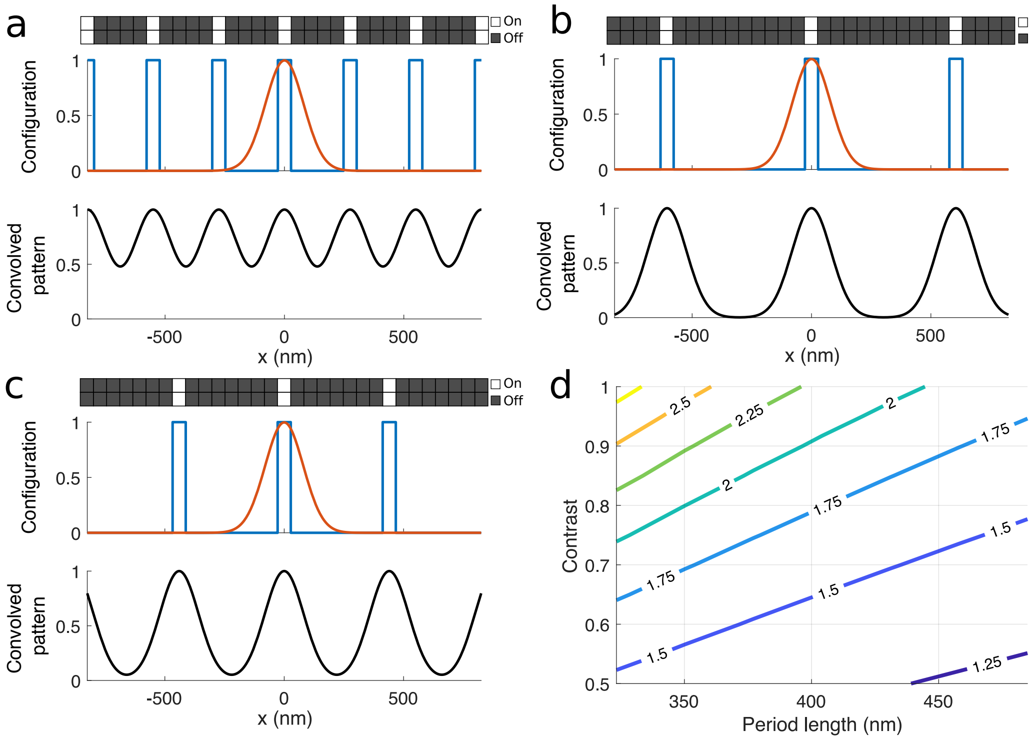

Supplementary Figure 11. Contrast and effective photon number of non-harmonic C-MELM implementation as a function of mirror configuration. (**a**) Theoretical 1D periodic illumination structure produced by a 1/5 duty cycle configuration of the DMD (top). The resulting intensity distribution after reflection (blue, equation (S38)) is convolved with the Gaussian PSF (red, equation (S39)), yielding the resulting illumination structure at the sample plane (black, equation (S40)). Due to the small separation distance between neighbouring mirror lines, the diffraction resulting from each mirror line overlaps with those of neighbouring mirrors. This produces a sinusoidal illumination structure with small period but poor contrast $C \approx 0.3$. (**b**) Same as **a**, here for a 1/11 duty cycle configuration. The large distance between neighbouring lines results in no overlap, producing large regions of constant intensity. While this illumination structure yields near-perfect contrast $C \approx 1$, the period is large. The lack of intensity gradient at large areas of the sample plane reduces the amount of information one can extract using C-MELM. (**c**) Same as **a** and **b**, here for a 1/8 duty cycle configuration. This specific distance between mirror lines results in very little overlap of the diffracted lines. This results in a close-to-sinusoidal high-contrast illumination structure of $C \approx 0.9$, illustrating the optimal mirror configuration in terms of the compromise between contrast and period. (**d**) $N_{\text{effective}}$ of C-MELM over optimal fitting of PSFs shown as a contour plot as a function of attained period and contrast, evaluated as the ratio of the two methods' CRLB. Increasing the contrast or reducing the period both allow for extraction of additional information from the structured illumination.

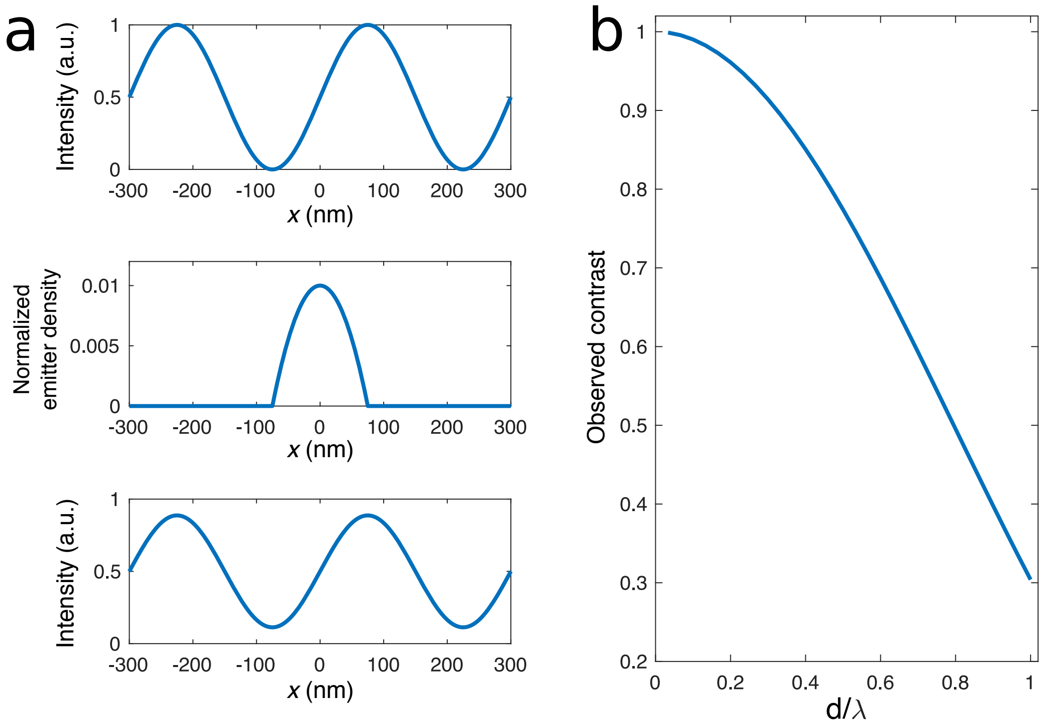

Supplementary Figure 12. Effect of particle size on measured structured illumination contrast. Simple theoretical evaluation of the effect of emitter size on characterized pattern contrast. (**a**) A harmonic intensity profile with perfect modulation contrast and period of $\lambda = 300$ nm (top) is characterized using a spherical particle (e.g. a fluorescent bead) of diameter d. Assuming a uniform distribution of small emitters within the particle volume, the normalized distribution of emitters along the x-axis is given by a simple projection of the spherical volume onto the x-axis (middle, here shown for a particle with d=150 nm). Each small emitter within the particle volume will emit an amount of photons proportional to the local intensity at its given position. Thus, the characterized illumination intensity at a given position is evaluated as a convolution of the intensity profile with the distribution of emitters (bottom), producing a characterized intensity profile with a reduced contrast compared to the actual intensity profile. (**b**) Calculated observed contrast as a function of the ratio between particle diameter d and the period of the harmonic intensity profile λ. Perfect contrast characterization is only achievable for sufficiently small particles, but particles that satisfy $d/\lambda < 0.2$ still obtain a $> 96\%$ accurate characterization of the contrast.

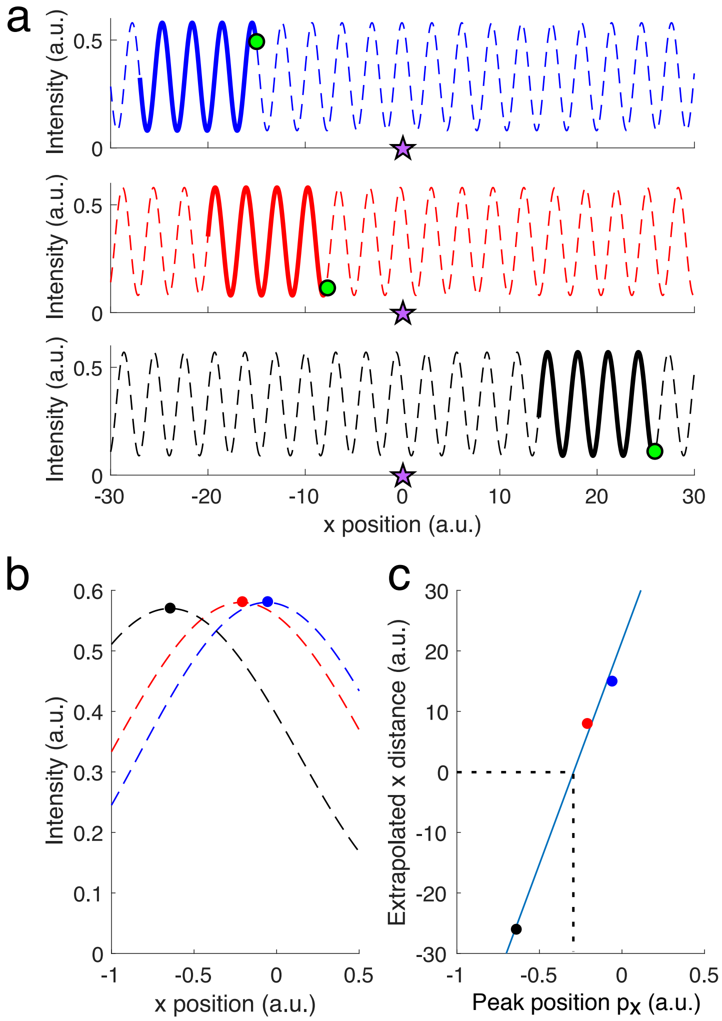

Supplementary Figure 13. Conceptual interpolation of illumination structures. For simplicity, the concept is here illustrated in 1D using the $n = 3$ nearest illumination structures. (**a**) Plot of $n = 3$ illumination structures (solid lines), nearest to the point-source of interest (purple star), and their extrapolation over the entire region of interest (dashed lines). Green dot indicates the starting point of each individual characterization measurement. Due to slight variations in fit parameters between the $n = 3$ characterizations (e.g. as a result of uncertainties or slow variations over the FOV), the extrapolated illumination structures are not identical, and thus predict varying positions of the intensity peak closest to the point-source of interest. (**b**) Zoom of **a** at the region close to the point-source of interest. Each illumination structure extrapolation predicts a slightly different position of the nearest peak in the actual illumination structure at the position of interest (coloured dots). (**c**) Extrapolated x-distance, i.e. difference in point-source position and starting point of each characterization, as a function of predicted peak position from **b**. The predicted peak positions are linear in the distance of extrapolation. Fitting a line to this data (blue line) thus allows for extraction of the estimated peak position of the actual illumination structure, i.e. at extrapolation distance 0 (dashed line). The resulting phase shift $\phi_{\text{int},x}$ of the actual illumination structure can then be calculated from equation (S45). Note that in the 2D case, this step involves fitting a plane instead of a line, as each characterized illumination structure is extrapolated in both the x- and y-direction (eq. (S43) and eq. (S44)).

Supplementary References

[1] Francisco Balzarotti, Yvan Eilers, Klaus C Gwosch, Arvid H Gynnå, Volker Westphal, Fernando D Stefani, Johan Elf, and Stefan W Hell. Nanometer resolution imaging and tracking of fluorescent molecules with minimal photon fluxes. *Science*, 355(6325):606–612, 2017.

[2] Jelmer Cnossen, Taylor Hinsdale, Rasmus Thorsen, Marijn Siemons, Florian Schueder, Ralf Jungmann, Carlas S. Smith, Bernd Rieger, and Sjoerd Stallinga. Localization microscopy at doubled precision with patterned illumination. *Nature Methods*, 17(1):59–63, 2020.

[3] G. A. Fry. Square-Wave Gratings Convoluted with a Gaussian Spread Function. *Journal of the Optical Society of America*, 58(10):1415–1416, 1968.

[4] Lusheng Gu, Yuanyuan Li, Shuwen Zhang, Yanhong Xue, Weixing Li, Dong Li, Tao Xu, and Wei Ji. Molecular resolution imaging by repetitive optical selective exposure. *Nature Methods*, 16(11):1114–1118, 2019.

[5] Kim I. Mortensen, L. Stirling Churchman, James A. Spudich, and Henrik Flyvbjerg. Optimized localization analysis for single-molecule tracking and super-resolution microscopy. *Nature Methods*, 7(5):377–381, 2010.

[6] Kim I. Mortensen and Henrik Flyvbjerg. "Calibration-on-the-spot": How to calibrate an EMCCD camera from its images. *Scientific Reports*, 6:28680, 2016.

[7] Kim I. Mortensen, Jongmin Sung, Henrik Flyvbjerg, and James A. Spudich. Optimized measurements of separations and angles between intra-molecular fluorescent markers. *Nature Communications*, 6:1–9, 2015.

[8] Kim I. Mortensen, Jongmin Sung, James A. Spudich, and Henrik Flyvbjerg. How to Measure Separations and Angles Between Intramolecular Fluorescent Markers. In Maria Spies and Yann R. Chemla, editors, *Methods Enzymol. Single-molecule enzymology: Fluorescence-Based and High-Throughput Methods*, volume 581, pages 147–185. Elsevier, 2016.

[9] C. Radhakrishna Rao. *Linear Statistical Inference and its Applications.* Wiley, 1973.

[10] Loïc Reymond, Johannes Ziegler, Christian Knapp, Fung-Chen Wang, Thomas Huser, Verena Ruprecht, and Stefan Wieser. SIMPLE: Structured illumination based point localization estimator with enhanced precision. *Optics Express*, 27(17):24578, 2019.